PNAS RESEARCH ARTICLE | ENGINEERING

High-temperature high-k polyolefin by rational molecular design

Jing Hao[a,1], Irene Mutegi[b,1], Madhubanti Mukherjee[c], Harikrishna Sahu[c], Ashish Khomane[b], Omer Yassin[b], Rampi Ramprasad[c], Gregory A. Sotzing[b,2], and Yang Cao[a,d,2]

Affiliations are included on p. 7.

Edited by David Weitz, Harvard University, Cambridge, MA; received July 30, 2024; accepted November 4, 2024

Polymer film dielectrics are highly favored for capacitive energy storage due to the inherent advantages of high breakdown strength, low dielectric loss, and ease of processing. High-density renewables conversion and harsh-condition electrification further emphasize the need for high-temperature, high-k polymers. A unique design strategy is developed to augment high-temperature polyolefins with improved dielectric constant, via the integration of phenyl pendants hanging off the rigid bicyclic backbone. The impacts of the pendant polarizability and steric positioning on dielectric constant, bandgap, glass-transition temperature (T_g), and high-field, high-temperature dielectric characteristics have been investigated. The orientational polarization of the polar phenyl pendants with rotational degree of freedom imparts cyclic olefins with enhanced dielectric constants, while maintaining the large bandgap, and high glass-transition temperature (T_g > 170 °C). Among these synthesized polymers, m-PNB-BP stands out with a remarkable dielectric constant of 4 at a high sub-T_g temperature of 150 °C, and a high discharged density of 8.6 J/m^3 at 660 MV/m. This study unveils a different path for designing high-temperature polymers with enhanced dielectric constants, particularly beneficial for capacitive energy storage.

high temperature | high dielectric constant | polymer | dielectric | energy storage

Significance

The development of high-temperature applications and the device miniaturization requests the polymer dielectrics shall ideally possess high dielectric strength at elevated temperatures with high discharged energy density and efficiency. However, almost all commercial polymers are bounded by the inverse correlation between bandgap and glass transition temperature/dielectric constant. In this work, a molecular design that integrates an enhanced dipole pendant to a rigid bicyclic backbone was proposed to establish high-temperature polymers with enhanced dielectric constants without sacrificing the bandgap. This work unlocks a unique rational design strategy of high-temperature high-k polymers for capacitor films.

Polymer dielectrics with notable attributes of high-voltage scalability, ease of processing, low dielectric loss, and graceful failure mode constitute key components of capacitive energy storage, filters, resonators, high-voltage (HV) isolators in electronic devices and electrical systems (1, 2). Enabled by the emerging wide-bandgap (WBG) power semiconductors (SiC, GaN) with higher blocking voltage, switching frequency, and higher temperature withstand than Si devices (IGBT, MOSFET), the rapid growth of harsh condition electrifications in (Hybrid) Electric Vehicles (H-EVs), More-Electric Aircraft (MEA), and down-hole oil/gas drilling and extractions has heightened the urgent needs of dielectrics operable under concurrent electric and thermal extremes (3–5). Furthermore, there are growing demands for device miniaturization with payload efficiency for offshore wind energies and mission critical applications like satellites, spacecraft, avionics systems, and combat vehicles. Therefore, polymer dielectrics shall ideally possess high dielectric strength at elevated temperatures with high discharged energy density and efficiency (6, 7). The energy density of linear dielectrics U_e can be estimated by

$$U_e = \frac{1}{2}\varepsilon_0\varepsilon_r E^2, \quad [1]$$

which can be enhanced by increasing the breakdown strength (E) or dielectric constant (ε_r). Currently, the highest breakdown strength for all-organic polymers is ~1 GV/m, with limited room for further improvement. Thus, increasing the polarization and hence the dielectric constant becomes a practically appealing approach. Moreover, it is crucial to consider dielectric loss, which comprises conduction loss and polarization loss, and forms during the charging and discharging processes (8). The dielectric loss dissipated in the form of heat, not only reduces the total delivered energy but also further increases the risk of failure due to thermal runaway. Notably, the dielectric loss will dramatically increase with the temperature and electric field, bringing in an obstacle for the operation of dielectrics in a harsh environment (8, 9). Therefore, charge-discharge efficiency plays a key factor when evaluating the dielectrics as a capacitor, especially at high temperatures and electric fields concurrently. Biaxially oriented polypropylene (BOPP) film has become the mainstream polymer dielectrics as capacitors, benefiting from its high breakdown strength and excellent charge-discharge efficiency. However, its relatively low dielectric constant (approximately 2.2) and the restricted maximum operating temperature (~90 °C) pose constraints on the overall energy density and capacity, hindering its capability to realize the miniaturization of electronic devices and

Author contributions: R.R., G.A.S., and Y.C. designed research; J.H., I.M., M.M., H.S., A.K., and Y.C. performed research; J.H., I.M., and A.K. contributed new reagents/analytic tools; J.H., I.M., M.M., H.S., A.K., O.Y., R.R., G.A.S., and Y.C. analyzed data; and J.H., I.M., M.M., R.R., G.A.S., and Y.C. wrote the paper.

The authors declare no competing interest.

This article is a PNAS Direct Submission.

[1]J.H. and I.M. contributed equally to this work.

[2]To whom correspondence may be addressed. Email: g.sotzing@uconn.edu or yang.cao@uconn.edu.

This article contains supporting information online at https://www.pnas.org/lookup/suppl/doi:10.1073/pnas.2415388121/-/DCSupplemental.

Published December 6, 2024.

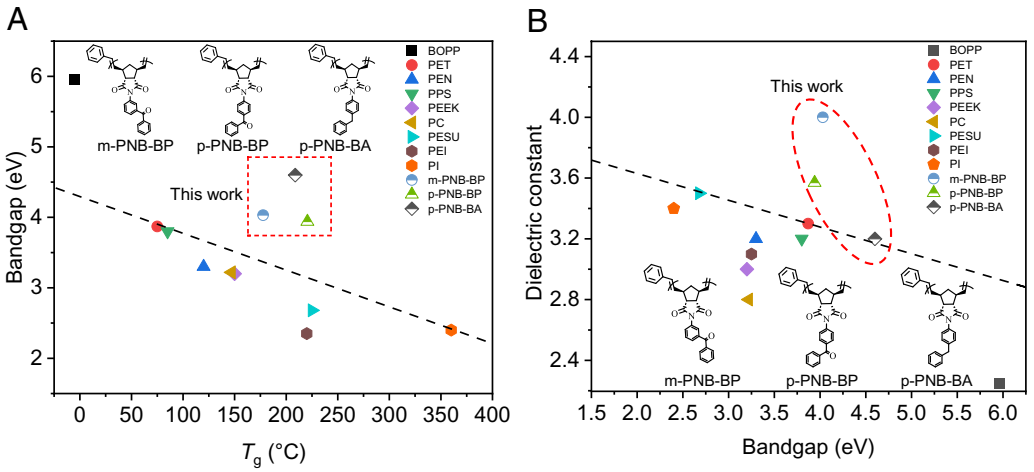

Fig. 1. The relationships between bandgap and T_g/dielectric constant for commonly used commercial capacitive polymers in comparison with m-PNB-BP, p-PNB-BP, and p-PNB-BA. (*A*) Relationship between bandgap and T_g. (*B*) Relationship between dielectric constant and bandgap.

electrical systems. Therefore, polymer dielectrics that possess a combination of high dielectric constants, high breakdown strength, low dielectric loss, and capacity to operate in elevated temperatures are urgently needed.

Various classes of polymer-based dielectrics exhibiting enhanced dielectric constants have been reported. Among these, one category is related to nanocomposites which are formed by the incorporation of high permittivity inorganic nanoparticles into the polymer matrix (10, 11). The dielectric constant of the nanocomposites is determined both by the nanoparticles and the polymers. However, the effective dielectric constant of nanocomposites will only arise with the filler loading significantly above the percolation threshold (12, 13), which often leads to the difficulty of film processing and the risk of establishing a conduction pathway due to interconnected particles (14). Moreover, the large contrast in dielectric constants between the nanoparticles and the polymers can enhance the local electric field, leading to a reduced breakdown strength for the nanocomposites (14–16). Another approach to obtain high dielectric constant polymers is to blend two or more types of polymers and generate an enhanced dielectric constant by changing the interchain spacing (17), but inappropriate blends can lead to issues of phase separation. Poly-(vinylidene fluoride) (PVDF)-based polymers and their copolymers have attracted attention in the pursuit of high dielectric constant dielectrics, primarily owing to the high polarity of the C—F bonds (18, 19). However, despite efforts such as relaxor ferroelectric engineering, the high hysteresis loss associated with the structural relaxation of the polymer main chain prevents their application as capacitor films (20, 21).

Meanwhile, T_g has emerged as a main proxy for evaluating the polymer dielectric performance. A high T_g polymer is preferred in general, to prevent the decline in mechanical integrity and the notable rise in dielectric loss in operation, especially at high temperatures (3). Commercial high T_g polymers, such as Polyimide (PI) boasting a T_g exceeding 310 °C, have found a wide range of applications such as electrical insulation (22) and high-temperature fuel cells (23). However, their thermal stability resides in the conjugated aromatic backbones, leading to diminishing bandgaps and hence high conduction loss and poor energy densities, especially at elevated temperatures (5, 24, 25). For example, the breakdown strength of PI at 150 °C is only 300 MV/m with a low charge-discharge efficiency of <40%.

A molecular engineering principle comprising repeat units of rigid fused bicyclic structure and alkenes, separated by freely rotating single bonds, was recently developed (3–5, 24, 26). While almost all commercial polymers are bounded by the inverse correlation between T_g and bandgap, as shown in Fig. 1*A*, newly designed polynorbornenes by this principle with rigid aliphatic bicyclic structures in the backbone all exhibit high T_g of >170 °C, together with high bandgaps of ≥4 eV. Additionally, this specific class of polynorbornenes, namely p-polynorbornene-benzophenone (p-PNB-BP), p-polynorbornene-benzylamine (p-PNB-BA), and m-polynorbornene-benzophenone (m-PNB-BP), feature specially designed phenyl pendant groups hanging off the bicyclic main-chain, with rotational degrees of freedom, to augment further the dipolar polarizations to achieve a high-k and hence a higher energy storage at high temperature, without compromising the bandgap (Fig. 1*B*). Systematic evaluation of the phenyl pendant groups, comprising carbonyl group or methylene linkages at meta- or para-position between two phenyl rings, was carried out to study their impacts on the dielectric polarization, bandgap, and T_g. The dipolar orientational polarization of these pendant groups and the implication of the steric hindrance were also investigated, along with the high-field, high-temperature characterizations. Among them, m-PNB-BP demonstrated a discharged density of 8.6 J/m^3 at 150 °C, due to its unyielding breakdown strength of 660 MV/m and high-k of 4 at high temperature.

Results and Discussion

The monomers were synthesized via thermal imidization, as depicted in Fig. 2*A*. Polymerization was achieved through ring-opening metathesis utilizing Grubbs 2nd generation catalyst, as illustrated in Fig. 2*B*. Distinguishing features among the three polymers primarily reside in two positions: the linkage connecting the two benzenes within the phenyl group and the position where the freely rotating pendant hangs off the backbone. The structures of the polymers were further confirmed by using NMR and Fourier transform infrared spectroscopy (FTIR), as shown in Fig. 2*C* and *SI Appendix*, Figs. S1–S3. In ^{1}H NMR of polymers (Fig. 2*C*), proton peaks between 7 ppm to 8 ppm characterize the pendant, with observable downfield shifts in the hydrogens of the pendant in p-PNB-BP and m-PNB-BP due to the electron-withdrawing functionalities of the carbonyl group. Wide-angle X-ray scattering (WAXS) analysis, depicted in Fig. 2*D* and *SI Appendix*, Fig. S4, reveals wide peaks indicative of the amorphous nature of all three polymers. The polymer films were made by solution casting using the Doctor Blade method, and transparent and free-standing films were obtained for further characterization (*SI Appendix*, Fig. S5).

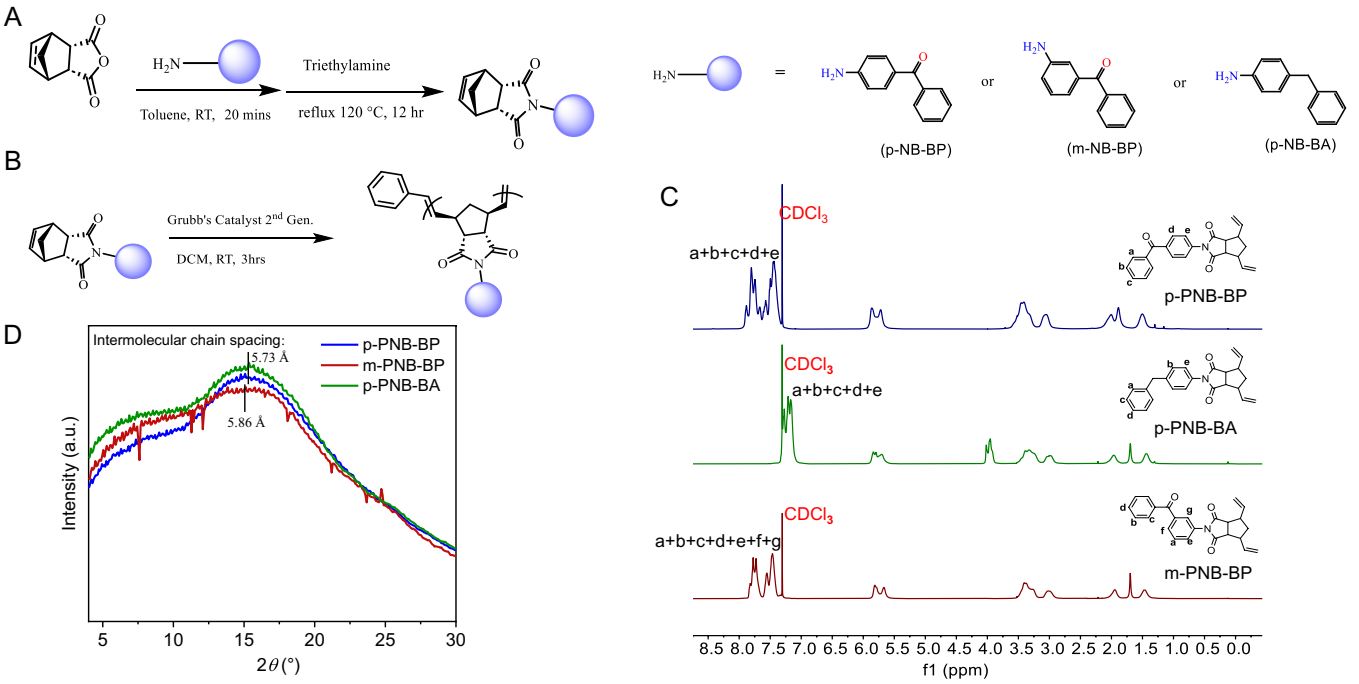

Fig. 2. Synthesis and structure characterization of p-PNB-BP, m-PNB-BP, and p-PNB-BA. (*A*) Synthesis process of monomers. (*B*) Polymerization process. (*C*) Comparisons of ^{1}H NMR. (*D*) WAXS results.

Dielectric Polarization. The temperature-dependent dielectric properties of p-PNB-BP, p-PNB-BA, and m-PNB-BP were characterized using dielectric spectroscopy, as shown in Fig. 3 *A*–*C*. Among these, m-PNB-BP exhibits the highest dielectric constants, while p-PNB-BA demonstrates the lowest. Specifically, at 20 °C and 1 kHz, the dielectric constants are approximately 3.2, 3.5, and 3.9 for p-PNB-BA, p-PNB-BP, and m-PNB-BP, respectively. At 150 °C and 1 kHz, the corresponding values are around 3, 3.3, and 4. While the dielectric constant of p-PNB-BA falls in line with those of commercial polymers, both p-PNB-BP and m-PNB-BP exhibit higher dielectric constants (Dk), with the Dk of m-PNB-BP reaching 4, nearly 2X of BOPP. As shown in Fig. 3 *A*–*C*, none of the PNBs shows relaxation loss due to glass-transition (α relaxation) at temperatures up to 150 °C, due to their high T_g of >170 °C. It shall be noted that p-PNB-BA has a different linkage between the two benzene groups in the phenyl pendant than p-PNB-BP and m-PNB-BP. p-PNB-BA utilizes methylene linkage, while p-PNB-BP and m-PNB-BP employ carbonyl groups. The electrophilicity of the carbonyl group attracts electrons in benzene toward it, making the two benzenes function as electron donors. It is corroborated by ^{1}H NMR results (Fig. 2*C*), showing a deshielding effect of the carbonyl group and lower electron density around the pendant hydrogens in p-PNB-BP and m-PNB-BP. Density functional theory (DFT) calculations further support this observation. The calculated electrostatic potential (Fig. 3*E*) reveals that in m-PNB-BP and p-PNB-BP, the electrophilicity of the carbonyl group and the presence of lone pair electrons induce negative potential around the linkage of the two benzenes, forming an enhanced dipole. Conversely, p-PNB-BA exhibits a positive region near the linkage due to carbon's relatively higher electronegativity than outward-facing hydrogen atoms. On the other hand, the difference in the linkage also leads to the different flexibility of pendant rotation, as supported by energy calculations for rotation around the N—C≡bond (Fig. 3*F*). The highest and lowest system energy corresponds to the most stable and the least stable states, respectively, and the difference between them ΔE is the maximum energy required for rotation. p-PNB-BA with methylene linkage has a higher ΔE than m-PNB-BP and p-PNB-BP which employ carbonyl groups, leading to a lower dielectric constant and potentially a higher thermal stability for p-PNB-BA.

Further comparison between m-PNB-BP, p-PNB-BP, and p-PNB-BA indicates that the position of pendant groups attached to the backbone influences dielectric constants. The higher dielectric constants of p-PNB-BP, and m-PNB-BP can be attributed to enhanced dipolar polarization of the carbonyl-containing phenyl pendant, via a "secondary" process of pendent group reorientation. m-PNB-BP with the pendant attached to the meta position shows a lower ΔE compared to p-PNB-BP with the pendant in the para position, indicating a higher flexibility and thus a higher dielectric constant. The nonaromatic bicyclic rigid main-chain ensures sufficiently high glass transitions that decouple these local reorientations from the "primary" main-chain relaxation, while providing the "carved-out" free volume to allow increased local reorientational freedom of dipoles with reduced dipole constraints and thus supporting a high discharge efficiency at high yet still below T_g temperatures. The imaginary permittivity (dissipation factor) of m-PNB-BP (Fig. 3*C*) undergoes a shift of the relaxation peak toward higher frequency with temperature increasing to a high sub-T_g temperature of 150 °C. While complicated cooperative chain vs side-group relaxation appears to present and requires further investigation, a low activation energy of 0.34 eV is estimated for this relaxation process, indicating the freedom of the dipole movement under an external field for m-PNB-BP. For para-linked p-PNB-BP, a lower net dipole moment was recorded, with hence only moderate polarization and Dk, due to the higher rotational symmetry for the pendent hanging off the N element. Overall, the polarization loss remains low even at 150 °C, due to ease of dipole movement which is local, uncorrelated, and decoupled from the main-chain movement that would only kick in at a higher temperature above T_g.

Bandgap. The bandgap of p-PNB-BP, p-PNB-BA, and m-PNB-BP was characterized by using UV-Vis spectroscopy (Fig. 4*A*). Benefitting from the rigid aliphatic bicyclic structure, all three polymers exhibit larger bandgaps than commercial

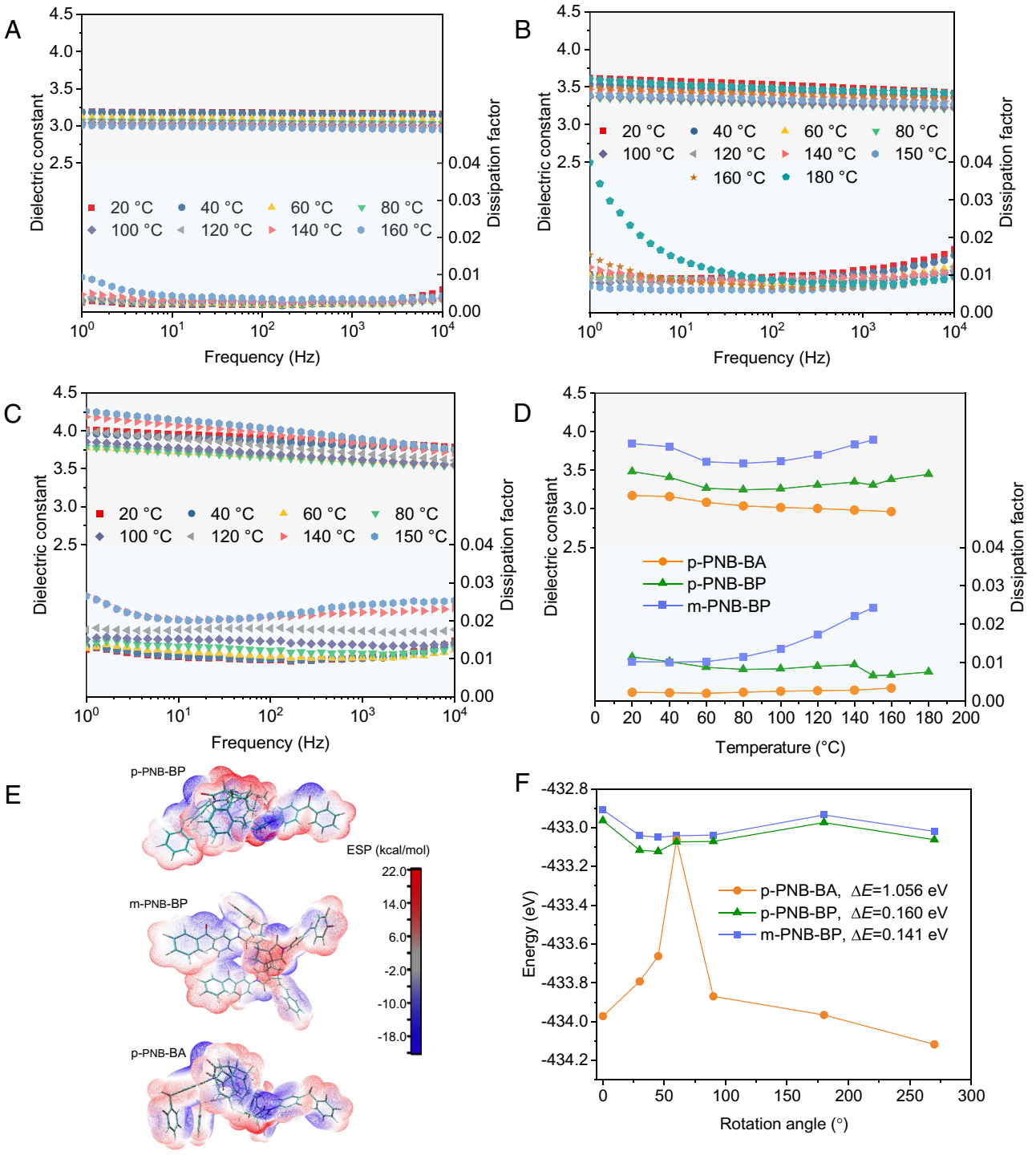

Fig. 3. Impacts of the polar group in the pendant and the position of the pendant attached to the backbone on the dielectric constants. Temperature-dependent dielectric spectroscopy of (*A*) p-PNB-BA, (*B*) p-PNB-BP, and (*C*) m-PNB-BP. (*D*) Temperature-dependent dielectric constant and dissipation factor of p-PNB-BA, p-PNB-BP, and m-PNB-BP at 1 kHz. (*E*) Calculated electrostatic potential of p-PNB-BP, m-PNB-BP, and p-PNB-BA. (*F*) Molecule energy of p-PNB-BA, p-PNB-BP, and m-PNB-BP with different dihedral angles between the pendant and the backbone.

high-temperature polymers, as shown in Fig. 1*A*. However, there is a notable trade-off when incorporating polar groups to enhance dielectric constants. While the presence of polar carbonyl groups can indeed increase dielectric constants, it can also lead to a compromised bandgap, as illustrated in Fig. 4 *A* and *B*. This compromise likely arises from induced separated energy states near the conduction band, as indicated in the calculated density of states (DOS) shown in Fig. 4*B*. Although these separated energy states near the conduction band may decrease the bandgap, they can form carrier traps and lead to trap modulated conduction. Notably, m-PNB-BP and p-PNB-BP stand out against commercial polymers, breaking the constraint of inverse relationship between dielectric constant and bandgap. Additionally, the position of pendant groups attached to the backbone also plays a role, although not prominent. Specifically, the meta position tends to result in a larger bandgap compared to the para position.

Glass Transition Temperature. T_g was determined using a differential scanning calorimetry (DSC). Due to the presence of the rigid backbone and aromatic side groups, all three systems

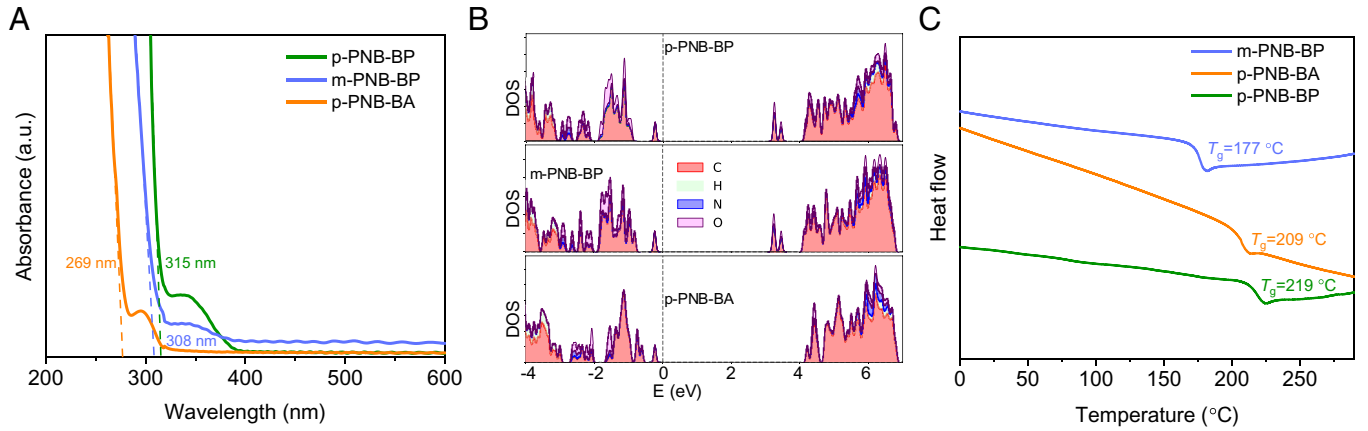

Fig. 4. Impacts of the polar group in the pendant and the position of the pendant attached to the backbone on the bandgap. (*A*) UV-vis spectra of p-PNB-BP, m-PNB-BP, and p-PNB-BA. (*B*) Calculated DOS of p-PNB-BP, m-PNB-BP, and p-PNB-BA. The dashed lines are tangents to obtain the onset wavelengths of absorption (*C*) DSC curves of p-PNB-BP, m-PNB-BP, and p-PNB-BA.

exhibit high T_g exceeding 170 °C. Specifically, the T_g of p-PNB-BP, p-PNB-BA, and m-PNB-BP are 219 °C, 209 °C, and 177 °C respectively, as shown in Fig. 4*C*. p-PNB-BP and p-PNB-BA show a higher T_g than m-PNB-BP owing to their tighter molecular packing and more restricted pendant rotation, as indicated in Figs. 2*D* and 3*F*. Moreover, the presence of highly polar carbonyl groups further enhances intermolecular interactions, leading to the highest T_g observed in p-PNB-BP. Remarkably, these polymers achieve high T_g values without significantly compromising their bandgap, breaking the typical inverse relationship seen

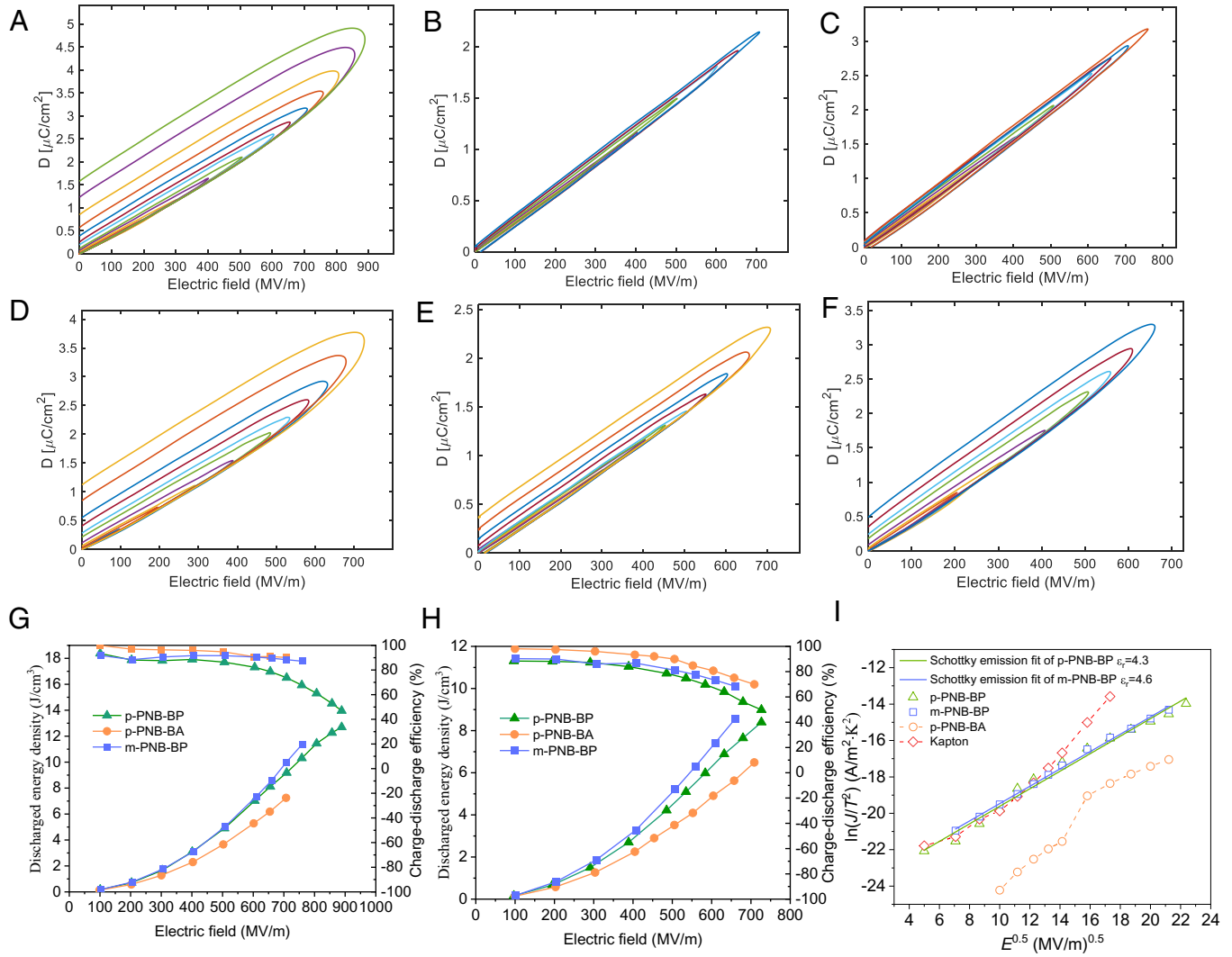

Fig. 5. Capacitive performance of p-PNB-BP, p-PNB-BA, and m-PNB-BP. (*A–C*) DE loops of (*A*) p-PNB-BP, (*B*) p-PNB-BA, and (*C*) m-PNB-BP at RT. (*D–F*) DE loops of (*D*) p-PNB-BP, (*E*) p-PNB-BA, and (*F*) m-PNB-BP at 150 °C. (*G* and *H*) Discharged energy density and charge-discharge efficiency of p-PNB-BP, p-PNB-BA, and m-PNB-BP at (*G*) RT and (*H*)150 °C. (*I*) Field-dependent current density of p-PNB-BP, m-PNB-BP, p-PNB-BA, and Kapton at 150 °C.

in commercial polymers, an exceptional character for excellent capacitive storage at elevated temperatures.

Capacitive Performance. The capacitive energy storage performance of p-PNB-BP, p-PNB-BA, and m-PNB-BP were evaluated at different temperatures, as shown in Fig. 5 *A*–*H*. At room temperature (RT), p-PNB-BP exhibits the highest field withstand, reaching a highest energy density U_d of 12.7 J/m^3 at 890 MV/m among the three polymers, despite noticeable losses at high fields. p-PNB-BA demonstrates the highest charge-discharge efficiency and it achieves an efficiency (η) of 90% at 707 MV/m with a U_d of 7.2 J/m^3. m-PNB-BP, with its high Dk and efficient charge-discharge performance, reaches a U_d of 11.4 J/m^3 at 760 MV/m with a decent η of 87%. All three polymers demonstrate excellent high-temperature dielectric characteristics and display notable breakdown strength (*SI Appendix*, Fig. S6). In particular, benefiting from its high dielectric constant, good charge-discharge efficiency, and satisfactory breakdown strength, m-PNB-BP achieves a U_d of 8.6 J/m^3 at 150 °C, with uncompromised high breakdown strength of 660 MV/m and Dk of 4.

Notably, while m-PNB-BP exhibits the highest loss factors in low-field dielectric spectroscopy, the losses at high fields remain insignificant, indicating an effective suppression of the conduction loss with its large bandgap, which would otherwise dominate in high electric fields. Fig. 5*I* shows the field-dependent current density of p-PNB-BP, p-PNB-BA, and m-PNB-BP at 150 °C, with Kapton included for comparison. The results show that p-PNB-BP and m-PNB-BP exhibit similar current densities to Kapton at fields below 200 MV/m. However, above this field, Kapton shows a sharp rise in current density, while p-PNB-BP and m-PNB-BP show only gradual increases. At 300 MV/m, the current density of p-PNB-BP and m-PNB-BP are approximately one-order-of magnitude lower than Kapton. In particular, p-PNB-BA shows the lowest leakage current, with current density about two orders of magnitude lower than those of Kapton, p-PNB-BP, and m-PNB-BP at fields below 200 MV/m, and more than two orders of magnitude lower than Kapton at 300 MV/m. The linearity of $\ln(J/T^2)$ versus $E^{0.5}$ for p-PNB-BP and m-PNB-BP suggests Schottky emission as the dominant conduction mechanism, with derived dielectric constants of 4.3 and 4.6, roughly consistent with the results from the dielectric spectroscopy. For p-PNB-BA, the linear $\ln(J)$ versus $\ln(E)$ relationship suggests a shift of space-charge-limited conduction mode from the trap-limited region to trap-"free" (trap-filled) region at 200 MV/m (*SI Appendix*, Fig. S7).

Materials and Methods

Synthesis.

Monomer synthesis. The same procedure was used in synthesizing p-PNB BP, m-PNB BP, and P-PNB-BA monomers. A 250 mL two-neck round-bottom flask fitted with a Dean-Stark trap and a condenser was flame-dried and purged with argon gas. The flask was charged with *cis*-5-Norbornene-endo-2,3-dicarboxylic anhydride (12.18 mmol) and (12.18 mmol) of either 4-aminobenzophenone, 3-aminobenzophenone, or 4-benzylamine. Anhydrous toluene (0.5 M based on the mole of the limiting reagent) was added to the flask via cannula transfer under argon gas. The mixture was stirred at room temperature for 20 min under argon. Triethylamine (12.18 mmol) was added dropwise to the reaction mixture and the reaction was refluxed in an oil bath at 120 °C for 12 h. After allowing the flask to cool at room temperature, dichloromethane was added to the reaction mixture and washed with Dilute HCl (5% v/v) followed by brine. The organic layer was dried over magnesium sulfate, filtered, and concentrated via rotovap to give an off-white solid. The product was recrystallized in ethanol to obtain a white imide crystal.

Polymer synthesis. The procedure applies to all polymers. The polymers were synthesized by ring-opening metathesis polymerization using Grubbs 2nd generation catalyst. The Polymer synthesis was carried out in a flame-dried 100 mL single-neck round-bottom flask under argon atmosphere. The monomer (3.0 mmol) was placed in the round bottom flask, and dichloromethane (10% w/v) was added using cannula transfer. Next, the monomer was dissolved in DCM using a magnetic stir bar. In a 20 mL vial, Grubbs 2nd generation catalyst (0.00265 mmol) was dissolved in anhydrous DCM (3.0 mL). Then, this catalyst solution was added to the monomer solution dropwise via cannula transfer under argon atmosphere. The reaction is allowed to proceed for 3 h at room temperature. The polymerization was terminated by adding ethyl vinyl ether (3.0 mL) and allowing it to stir for 20 min. The reaction mixture was added dropwise to methanol (~150 mL) with continuous stirring. The precipitated polymer was collected via filtration. Then, it was redissolved in dichloromethane and added dropwise to methanol (~150 mL) under continuous stirring. The polymer was further purified through Soxhlet extraction using methanol and dried under vacuum at 60 °C for 24 h to obtain a pure white polymer.

Film Processing. The polymer film was made by solution casting using Doctor Blade method. Polymer was dissolved in N,N-Dimethylacetamide (DMAc) solvent with 10% (W/W) concentration. Then, the solution was filtered through a 0.45-micron GPC filter. The filtrate was cast on a glass substrate preheated at 40 °C using a 380 microns applicator. The cast wet film is then allowed to dry at 40 °C for 2 h and then at room temperature for 12 h. The film is then peeled from the glass substrate using DI water to obtain a flexible freestanding polymer film. The film was dried under a vacuum at 80 °C for three days.

Characterization. ^{1}H and ^{13}C NMR characterization for polymers and monomers was carried out using Bruker AVANCE 500 MHz spectrometer with TMS as an internal standard. Fourier-transform infrared spectroscopy (FTIR) was performed using Thermo Fisher Nicolet Magna 560 IR spectrometer. For the measurement of glass transition temperature (T_g), TA Instruments DSC Q-20 differential scanning calorimeter was used. The polymer sample is subjected to two heating and one cooling cycle at the rate of 10 °C/min. The T_g mentioned is recorded from the second heating cycle. TA instruments TGA Q-500 was used to perform thermogravimetric analysis. The polymer is heated from 25 °C to 750 °C at the rate of 10 °C/min. Polymer degradation temperature is obtained from TGA analysis. The molecular weight of the synthesized polymers is determined using Waters GPC system with dimethylacetamide (DMAc) as a mobile system and polystyrene as a standard. UV/VIS/NIR-Perkin Elmer Lambda 1050 was used to measure bandgap energy on a dried free-standing film. WAXS analysis was performed using an Oxford Xcalibur diffractometer equipped with a CCD detector and Cu Kα radiation (λ=1.5418 Å) operated at 35 kV and 35 mA.

High-Field Dielectric Testing. High field displacement–electric field loop measurement: The electric displacement-electric field (D-E) loops were assessed using a modified Sawyer-Tower polarization loop tester, employing a unipolar positive half sinusoidal wave at a frequency of 100 Hz. The measurement setup comprised a Trek Model 10/40 10 kV high voltage amplifier, in conjunction with an OPA541 operational amplifier-based current-to-voltage converter. To ensure effective contact between the electrodes and the film, gold/palladium electrodes, each with a diameter of 3 mm, were applied to both sides of the film utilizing the sputter coating technique.

High-field conduction measurement: For leakage current measurements, a high voltage was applied using a Stanford Research PS365 power supply, while the currents were recorded with a Keithley 6,514 electrometer. Gold/palladium electrodes, with a diameter of 3 mm, were deposited on the sample surface.

Breakdown test: A ramp voltage with a rise rate of 250 V/s was applied through Stanford Research PS365 power supply. Gold/palladium electrodes, with a diameter of 3 mm, were deposited on the sample surface.

Dielectric Spectroscopy. Dielectric spectroscopy measurements were performed using a Solartron SI 1,260 frequency response analyzer paired with a Solartron 1,296 dielectric interface. The sample under test was housed within a test cell and subjected to controlled temperature conditions facilitated by a Delta Design 9,015 temperature controller. To enable intimate contact between the electrode and the dielectric, gold/palladium electrodes with a diameter of 30 mm were coated onto the sample.

DFT Calculation. All the systems were modeled as oligomers using PSP with three repeat units to optimize the computational cost (27). The structures were successfully optimized by using Perdew–Burke–Ernzehof (PBE) functional with

generalized gradient approximation (GGA) scheme employing conjugate gradient algorithm (CGA), as implemented in VASP, with strict criteria of the forces on each atom being less than 0.0002 eV/Å. The energy cut-off was set to 500 eV for all the systems. After the optimization, the structures were further converged by using strict energy convergence criteria of 10^{-6} eV to ensure accuracy. To obtain an accurate density of states, the Heyd–Scuseria–Ernzerhof hybrid density functional (HSE06) was used (28). In the hybrid functional, range separation and mixing parameters of 0.2 $Å^{-1}$ and 0.25 were used. Electronic properties for all exchange–correlation functionals were calculated using a tetrahedron method with Blöchl corrections, where the smearing width of 0.02 eV was used. We have used 20000 grid points to evaluate the density of states. The D3 corrections were added for all the calculations.

The optimized geometries were subjected to single-point calculations using dispersion-corrected PBE0 (PBE0-D3) functional employing a double-zeta basis set: def2-SVP. Becke−Johnson damping (29) was utilized with the D3 dispersion model in PBE0-D3. These calculations were carried out using the Orca 5.0 program (30). Electrostatic potential (ESP) surface plots were generated by using Multiwfn (31) and VMD (32).

Data, Materials, and Software Availability. All study data are included in the article and/or *SI Appendix*.

ACKNOWLEDGMENTS. This work was supported through a Multidisciplinary University Research Initiative (MURI) Grant (No. N00014-17-1-2656) and a capacitor program Grant (No. N0014-19-1-2340), both from ONR. We would like to thank Dr. Mayra Daniela Morales-Acosta for the wide-angle X-ray scattering (WAXS) measurements.

Author affiliations: [a]Electrical Insulation Research Center, Institute of Materials Science, University of Connecticut, Storrs, CT 06269; [b]Institute of Materials Science, University of Connecticut, Storrs, CT 06269; [c]School of Materials Science and Engineering, Georgia Institute of Technology, Atlanta, GA 30332; and [d]Department of Electrical and Computer Engineering, University of Connecticut, Storrs, CT 06269

1. A. Mannodi-Kanakkithodi *et al.*, Rational Co-design of polymer dielectrics for energy storage. *Adv. Mater.* **28**, 6277–6291 (2016).
2. M. Rabuffi, G. Picci, Status quo and future prospects for metallized polypropylene energy storage capacitors. *IEEE Trans. Plasma Sci.* **30**, 1939–1942 (2002).
3. A. A. Deshmukh *et al.*, Flexible polyolefin dielectric by strategic design of organic modules for harsh condition electrification†. *Energy Environ. Sci.* **15**, 1307–1314 (2022).
4. C. Wu *et al.*, Flexible cyclic-olefin with enhanced dipolar relaxation for harsh condition electrification. *Proc. Natl. Acad. Sci. U.S.A.* **118**, e2115367118 (2021).
5. C. Wu *et al.*, Rational design of all-organic flexible high-temperature polymer dielectrics. *Matter* **5**, 2615–2623 (2022).
6. Q. Zhang, X. Chen, T. Zhang, Q. M. Zhang, Giant permittivity materials with low dielectric loss over a broad temperature range enabled by weakening intermolecular hydrogen bonds. *Nano Energy* **64**, 103916 (2019).
7. T. Zhang *et al.*, A highly scalable dielectric metamaterial with superior capacitor performance over a broad temperature. *Sci. Adv.* **6**, eaax6622 (2020).
8. T. W. Dakin, Conduction and polarization mechanisms and trends in dielectric. *IEEE Electr. Insul. Mag.* **22**, 11–28 (2006).
9. H. Shirakawa, T. Ito, S. Ikeda, Electrical properties of polyacetylene with various *cis-trans* compositions. *Die Makromol. Chem.* **179**, 1565–1573 (1978).
10. X. Zhang *et al.*, Ultrahigh energy density of polymer nanocomposites containing $BaTiO_3$ @TiO_2 nanofibers by atomic-scale interface engineering. *Adv. Mater.* **27**, 819–824 (2015).
11. Z. Pan *et al.*, Simultaneously enhanced discharge energy density and efficiency in nanocomposite film capacitors utilizing two-dimensional $NaNbO_3$ @Al_2O_3 platelets. *Nanoscale* **11**, 10546–10554 (2019).
12. S. A. Ling An, J. P. Boggs, Calame, Energy storage in polymer films with high dielectric constant fillers. *IEEE Electr. Insul. Mag.* **24**, 5–10 (2008).
13. J. P. Calame, Finite difference simulations of permittivity and electric field statistics in ceramic-polymer composites for capacitor applications. *J. Appl. Phys.* **99**, 084101 (2006).
14. L. Zhu, Exploring strategies for high dielectric constant and low loss polymer dielectrics. *J. Phys. Chem. Lett.* **5**, 3677–3687 (2014).
15. J. Wang *et al.*, Achieving high electric energy storage in a polymer nanocomposite at low filling ratios using a highly polarizable phthalocyanine interphase. *J. Polym. Sci. B Polym. Phys.* **52**, 1669–1680 (2014).
16. Z. Pan, L. Yao, J. Zhai, X. Yao, H. Chen, Interfacial coupling effect in organic/inorganic nanocomposites with high energy density. *Adv. Mater.* **30**, 1705662 (2018).
17. Y. Thakur *et al.*, Generating high dielectric constant blends from lower dielectric constant dipolar polymers using nanostructure engineering. *Nano Energy* **32**, 73–79 (2017).
18. H. S. Nalwa, Ed., *Ferroelectr. Polym.* (CRC Press, 1995).
19. A. J. Lovinger, Ferroelectric polymers. *Science* **220**, 1115–1121 (1983).
20. V. Bobnar *et al.*, Dielectric properties of relaxor-like vinylidene fluoride−trifluoroethylene-based electroactive polymers. *Macromolecules* **36**, 4436–4442 (2003).
21. B. Chu *et al.*, A dielectric polymer with high electric energy density and fast discharge speed. *Science* **313**, 334–336 (2006).
22. H. Sun *et al.*, Insulation characteristics of polyimide as insulation material used in pancake tape coil structure for resistive-type SFCL. *IEEE Trans. Appl. Supercond.* **25**, 1–4 (2015).
23. Y. Jin, R. Liu, X. Che, T. Wang, J. Yang, New high temperature polymer electrolyte membranes based on poly(ethylene imine) crosslinked poly(ether ketone cardo). *J. Electrochem. Soc.* **168**, 054524 (2021).
24. C. Wu *et al.*, Flexible temperature-invariant polymer dielectrics with large bandgap. *Adv. Mater.* **32**, 2000499 (2020).
25. J. Chen *et al.*, Aromatic-free polymers based all-organic dielectrics with breakdown self-healing for high-temperature capacitive energy storage. *Adv. Mater.* **35**, e2306562 (2023).
26. C. Wu *et al.*, Remarks on the design of flexible high-temperature polymer dielectrics for emerging grand electrification–Exemplified by Poly(oxa)norbornenes. *IEEE Trans. Die. Electr. Insul.* **28**, 1468–1470 (2021).
27. H. Sahu, K.-H. Shen, J. H. Montoya, H. Tran, R. Ramprasad, Polymer Structure Predictor (PSP): A python toolkit for predicting atomic-level structural models for a range of polymer geometries. *J. Chem. Theory Comput.* **18**, 2737–2748 (2022).
28. J. Heyd, G. E. Scuseria, M. Ernzerhof, Hybrid functionals based on a screened Coulomb potential. *J. Chem. Phys.* **118**, 8207–8215 (2003).
29. S. Grimme, S. Ehrlich, L. Goerigk, Effect of the damping function in dispersion corrected density functional theory. *J. Comput. Chem.* **32**, 1456–1465 (2011).
30. F. Neese, Software update: The ORCA program system–Version 5.0. *WIREs Comput. Mol. Sci.* **12**, e1606 (2022).
31. T. Lu, F. Chen, Multiwfn: A multifunctional wavefunction analyzer. *J. Comput. Chem.* **33**, 580–592 (2012).
32. W. Humphrey, A. Dalke, K. Schulten, VMD: Visual molecular dynamics. *J. Mol. Graph.* **14**, 33–38 (1996).